Dynamic elastic response of $KMn_{1-x}Ca_xF_3$: Elastic softening and domain freezing

W. Schranz* and P. Sondergeld
Nonlinear Physics Group, Faculty of Physics, University of Vienna, Boltzmanngasse 5, A-1090 Wien, Austria

A. V. Kityk
Institute for Computer Science, Czestochowa University of Technology, Armii Krajowej 17, PL 42-200 Czestochowa, Poland

E. K. H. Salje
Department of Earth Sciences, University of Cambridge, Downing Street, Cambridge CB2 3EQ, United Kingdom
(Received 23 June 2009; revised manuscript received 1 September 2009; published 25 September 2009)

Results of continuous-wave resonance (MHz-region) and ultralow-frequency (Hz-region) dynamic mechanical analyzer measurements of pure $KMnF_3$ and mixed crystals $KMn_{1-x}Ca_xF_3$ ($x<0.017$) are presented in a broad temperature range including the phase-transition regions. The elastic anomalies depend strongly on the measurement frequency: The MHz-elastic constants can be well fitted by Landau theory including the difference between isothermal and adiabatic behavior. Contrary, at low frequencies (0.1–50 Hz) an elastic softening (superelasticity) due to domain-wall motion is found quite similar to that observed recently in isostructural $SrTiO_3$ [A. V. Kityk *et al.*, Phys. Rev. B **61**, 946 (2000)]. However, unlike to $SrTiO_3$, for the mixed system $KMn_{1-x}Ca_xF_3$ we have measured freezing of the domain-wall movement around 100 K in a certain range of concentration of Ca^{2+} ions ($x=0.003$). Calculating the dynamic elastic response to the ac-stress field by taking into account the motion of randomly pinned ferroelastic domain walls in $KMn_{1-x}Ca_xF_3$ yields excellent agreement between theory and experiment.

DOI: 10.1103/PhysRevB.80.094110 PACS number(s): 62.40.+i, 61.72.Mm, 68.35.Ja, 64.70.K−

I. INTRODUCTION

Perovskites (ABO_3) display a wide variety of physical properties, such as superconductivity, magnetism, and ferroelectricity making them very interesting for applications in material sciences. In the geological context, the elastic and seismic properties of minerals such as those with perovskite structure are important for the understanding of the structure of the deep earth mantle. While much work has been done in this field a main shortcoming is that high-frequency data are often simply transferred to the seismologically important low-frequency range without consideration of the physical reasons, e.g., their microstructures, for frequency dispersion.[1,2]

Strong dispersion exists particularly in the precursor softening of perovskites.[3] In order to clarify such dispersion effects—so far measured on different samples—it is desirable to measure the frequency dependence of elastic moduli using the same crystal in two very different frequency ranges.

Here we present the results of continuous-wave resonance (CWR) (MHz-region) and ultralow-frequency (Hz-region) elastic measurements of mixed fluorperovskite $KMn_{1-x}Ca_xF_3$ ($x\leq 0.017$) as a function of temperature, frequency and applied stress. Ultrasonic elastic constants in pure $KMnF_3$ crystals have been repeatedly measured (see, e.g., Refs. 4–7) whereas measurements on mixed crystals are rare. Therefore it is quite natural to study the influence of Ca^{2+} ions on the elastic properties of mixed $KMn_{1-x}Ca_xF_3$. This work was also motivated by our former results on the low-frequency elastic behavior of isostructural $SrTiO_3$ crystals[8,9] where we have observed a distinct elastic softening ("superelasticity") below the cubic→tetragonal phase transition at $T_{c1}=105$ K. The superelasticity in $SrTiO_3$, which appears only in the Hz regime, is caused by the motion of ferroelastic domain walls and can be suppressed by an external uniaxial stress. Dispersion occurs also in this regime because the isothermal and adiabatic conditions lead to a crossover for typical sample sizes at several Hz.

As we shall show below, similar superelastic behavior is also found for pure $KMnF_3$ and mixed compounds. However, in contrast to $SrTiO_3$, where the domain walls have been observed to be mobile down to the lowest measured temperatures (10 K),[9] the system $KMn_{1-x}Ca_xF_3$ shows a quite different behavior,[3,10] i.e., some domain-wall motion freezes at low temperatures both in $KMnF_3$ (160 K in $KMnF_3$) and in mixed crystals (e.g., $T_V\approx 55$ K) in a certain range of concentration of Ca^{2+} ions. In comparison, almost complete domain freezing was observed previously in $LaAlO_3$.[11] Our current observations are a complete characterization (at low and high frequencies) of the elastic properties of a fluorperovskite.

Phase Transitions in $KMn_{1-x}Ca_xF_3$

Pure $KMnF_3$ undergoes a sequence of phase transitions related to the rotation of octahedral MnF_6 groups.[12] The parent phase (phase I) forms a perovskite structure with cubic space group O_h^1 ($Pm3m$). The high-temperature transition of $KMnF_3$ at $T_{c1}=186.5$ K, which is accompanied by a symmetry reduction $Pm3m\rightarrow I4/mcm$, is weakly first order,[13] i.e., close to a tricritical point.[14] From a structural point of view, this phase transition is identical to the cubic-tetragonal transition in $SrTiO_3$. It can be classified as an improper ferroelastic transition with an instability of the R_{25} soft mode at the [111] point of the Brillouin-zone boundary.[12] This mode is associated with the rotation of MnF_6 octahedra around the

[001] axis which becomes the tetragonal c_t axis below T_{c1} (phase II). Accordingly, the rotation angle ϕ of these octahedra can be chosen as the primary order parameter for the tetragonal phase (phase II), i.e., $\eta \propto \phi$. At low temperatures two other successive phase transitions occur at $T_{c2}=91$ K (phase III) and $T_N=88$ K (phase IV).[15–18] The structural phase transition at T_{c2} involves the softening of phonons of M_3 symmetry. This results in an orthorhombic *Pnma* phase (phase III) in which the octahedra are still rotated around the previous tetragonal c_t axis and slightly rotated around one of the pseudotetragonal a_t axes.[19] However, Kapusta *et al.*[20] found some evidence that phase III has monoclinic $P2_1/m$ symmetry. Below the Néel temperature $T_N=88$ K (phase IV) an antiferromagnetic ordering of the Mn network develops.[15,16] The critical behavior of pure $KMnF_3$ single crystals around the antiferromagnetic phase transition at T_N (Ref. 21) was studied by simultaneous measurements of the specific heat, thermal conductivity, and thermal diffusivity. The critical exponent and amplitude ratio of thermal diffusivity and specific heat agree with the predictions of the three-dimensional Heisenberg model for isotropic magnets. Another tetragonal (or pseudo-orthorhombic) phase (phase V) was reported to occur below $T_{c3}=82$ K (Refs. 17 and 18) and has magnetic properties ("canted antiferromagnet").

Gibaud *et al.*[18] performed high-resolution x-ray-diffraction measurements of the lattice parameters as a function of temperature for the mixed system $KMn_{1-x}Ca_xF_3$ in the concentration range $x \leq 0.05$. The temperature dependence of the lattice parameters in doped $KMn_{1-x}Ca_xF_3$ is similar to the one measured in pure $KMnF_3$. However, the temperatures of all phase transitions are enhanced by the substitution of Ca^{2+} for the Mn^{2+} ions.[22,23] It was argued[24,25] that the increase in T_c with Ca content is the consequence of the larger ionic radius of the Ca^{2+} ions [$R(Ca^{2+})=1.0$ Å and $R(Mn^{2+})=0.83$ Å since it is in high spin state[26]] which forces a displacement of the fluorines off their symmetry positions and stabilizes the lower symmetry phase. We will show below that this mechanism also seems to create (100) dumbbell fluorine interstitials which could serve as pinning centers for the ferroelastic domain walls. A remarkable peculiarity of the mixed system $KMn_{1-x}Ca_xF_3$ is a continuous temperature dependence of the lattice parameters in the vicinity of T_{c1} appearing at higher Ca concentrations.[18] Accordingly the $x-T$ phase diagram of $KMn_{1-x}Ca_xF_3$ contains a tricritical point. This conclusion was recently confirmed by a calorimetric and order-parameter study, where the critical composition was determined to be near $x_t=0.5$ mol % Ca.[23] A tricritical behavior has been also revealed earlier[27] in pure $KMnF_3$ under uniaxial pressure applied along [100] and [110].

II. EXPERIMENT

The $KMn_{1-x}Ca_xF_3$ samples were prepared using the Bridgman-Stockbarger method at Université du Maine (Le Mans, France). The resulting crystals were approximately cylindrical, with a thickness of 5 mm and circular (001) faces with an area of about 1 cm^2. The pure $KMnF_3$ samples did not show any trace of calcium by electron microprobe analysis. The doped samples had Ca concentrations of 0.3 mol % and 1.7 mol %. The samples are identical with those used previously by Gibaud *et al.*,[18] Romero *et al.*,[23] Gallardo *et al.*,[22] and Salje *et al.*[3] so that a direct comparison with their results is possible.

The temperature dependence of the high-frequency elastic constants was measured using the CWR technique.[28] Standing waves are set up in a composite oscillator consisting of a transducer, a coupling glycerol film, and the sample by applying a sinusoidally varying voltage to the transducer. The sound velocity v_s is obtained in terms of sample length l_s and resonance frequency f_n according to the formula

$$v_s = 2l_s f_n/n, \tag{1}$$

where n is the corrected value on the order of resonance, which according to Ref. 28 can be determined as

$$n = \frac{f_n + (\rho_T l_T/\rho_s l_s)(f_n - f_T)}{\Delta f[1 + (\rho_T l_T/\rho_s l_s)]}. \tag{2}$$

Here ρ_T (4.633 g/cm^3) and ρ_s (3.41 g/cm^3) are the $LiNbO_3$ transducer and sample densities, respectively, l_T is the transducer thickness and Δf is the frequency interval between two neighboring resonances. Since the resonance frequencies of the composite oscillator correspond to the maxima of the impedance, the sound velocity in the sample can be determined by measuring the impedance as a function of frequency. Longitudinal and transverse acoustic waves were excited via $LiNbO_3$ transducers with resonance frequency $f_T=15$ MHz. The impedance of the composite oscillator was measured with an HP 4192ALF impedance analyzer and the temperature was controlled with a He closed-cycle cryostat. The typical thickness of the samples for continuous-wave resonance measurements was about 2 mm. Under such experimental conditions the absolute accuracy is about 2–3 %, whereas the relative one is about 0.05%.

For the low-frequency elastic measurements a dynamical mechanical analyzer (DMA7-Perkin Elmer) was used. The samples are exposed to a given static force which is modulated by a dynamic force of chosen amplitude and frequency ($f=0.1-50$ Hz). The force can be tuned between 1 mN and 2.5 N. The amplitude u and the phase shift δ of the resulting elastic response of a sample are registered via inductive coupling with a resolution of $\Delta u \approx 10$ nm and $\Delta\delta \approx 0.1°$. The knowledge of δ and u allows the determination of both real and imaginary parts of the complex elastic compliance $S^*(\mathbf{n})=S'(\mathbf{n})+iS''(\mathbf{n})$ in $\mathbf{n}$ direction of the sample, where $S'(\mathbf{n})=|S^*(\mathbf{n})|\cos\delta$ and $S''(\mathbf{n})=|S^*(\mathbf{n})|\sin\delta$. Measurements have been performed by a parallel-plate stress (PPS) method (see Fig. 1 from Ref. 9) yielding

$$S^*(\mathbf{n}) = \frac{A}{F}\frac{u}{h}(\cos\delta + i\sin\delta), \tag{3}$$

where h and A represent the sample thickness and area, respectively, and F is the magnitude of the applied force. In our studies we used samples with typical dimensions $A \approx 1$ mm^2 and $h \approx 3$ mm. The absolute accuracy of such measurements is usually not better than 20%, whereas the relative accuracy of the DMA method is within 0.2–1 %. For

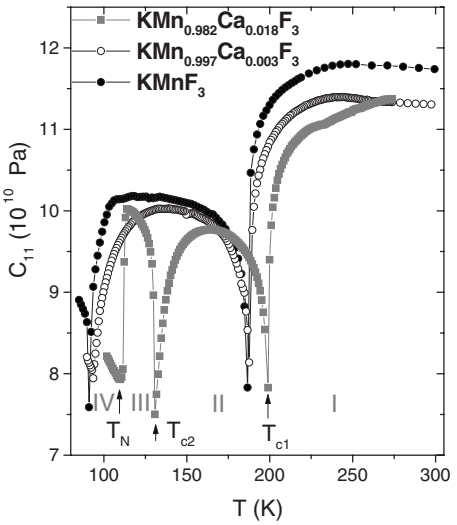

FIG. 1. Temperature dependence of C_{11} of $KMn_{1-x}Ca_xF_3$ for $x=0$, 0.003, and 0.017 determined by the CWR method at $f=15$ MHz for longitudinal mode with propagation vector $\mathbf{q}\|[100]$ and polarization $\mathbf{e}\|[100]$.

more details of the method and its application for the investigation of phase transitions see, e.g., Refs. 29 and 30.

Note that our parallel-plate geometry is different from the three-point-bending geometry of Salje and Zhang[3] who used a very thin plate and observed the bending of the plate rather than the compression of the parallelepiped.

III. EXPERIMENTAL RESULTS

A. Elastic properties in the MHz region

Figures 1–3 show the temperature dependences of the elastic constants C_{11}, $C_{\text{eff}}=\frac{1}{2}(C_{11}+C_{13})+C_{55}$ and C_{44} of

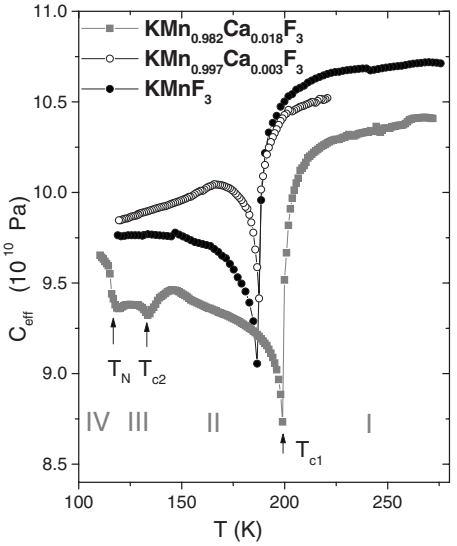

FIG. 2. Temperature dependence of $C_{\text{eff}}=\frac{1}{2}(C_{11}+C_{13})+C_{55}$ of $KMn_{1-x}Ca_xF_3$ for $x=0$, 0.003, and 0.017 determined by the CWR method at $f=15$ MHz for a longitudinal mode with propagation vector $\mathbf{q}\|[101]$ and polarization $\mathbf{e}\|[101]$.

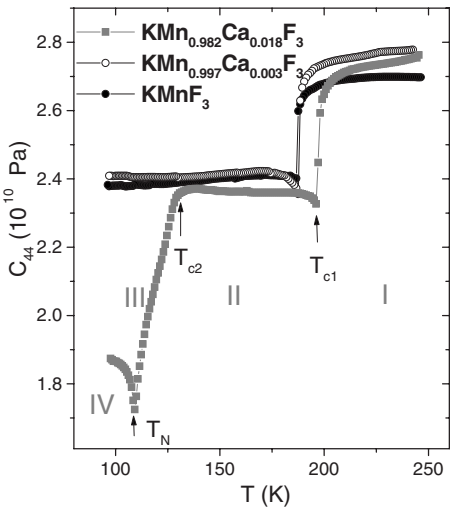

FIG. 3. Temperature dependence of C_{44} of $KMn_{1-x}Ca_xF_3$ for $x=0$, 0.003, and 0.017 determined by the CWR method at $f=15$ MHz for transverse mode with propagation vector $\mathbf{q}\|[100]$ and polarization $\mathbf{e}\|[010]$.

$KMn_{1-x}Ca_xF_3$ calculated from the velocities measured by the CWR method at 15 MHz

$$C_{11}=\rho_s V^2_{q\|[100],e\|[100]},$$

$$\frac{1}{2}(C_{11}+C_{13})+C_{55}=\rho_s V^2_{q\|[101],e\|[101]},$$

$$C_{44}=\rho_s V^2_{q\|[100],e\|[010]}, \quad (4)$$

where $\mathbf{q}$ and $\mathbf{e}$ indicate the wavevector and polarization of the acoustic wave, respectively.

One observes that the substitution of Ca^{2+} for Mn^{2+} ions does not change the qualitative character of the elastic behavior near the individual phase transitions. As already mentioned above, all phase transitions are shifted to higher temperatures with increasing Ca^{2+} content. Therefore in Figs. 2 and 3 two more elastic anomalies at T_{c2} and T_N show up for $x=0.017$ as compared to $x=0$ and $x=0.003$. Figure 1 shows the onset of the phase transition at T_{c2} also for $x=0.003$ and $x=0$. Concerning the phase transition at T_{c1} the temperature dependence of all elastic constants in doped $KMn_{1-x}Ca_xF_3$ appears to be very similar to those measured in pure $KMnF_3$ and there is good agreement with the results of previous acoustic measurements for pure $KMnF_3$.[4,6] A continuous decrease in the region of the cubic-tetragonal transition at T_{c1} occurs in all elastic constants. A similar anomaly is observed also for C_{11} near the transition from the tetragonal phase II to the orthorhombic phase III at T_{c2}. C_{eff} (Fig. 2) undergoes only a weak decrease at the transition temperature T_{c2}, whereas the temperature behavior of C_{44} displays a clear kink (Fig. 3) at this temperature. The transition to the low-temperature phase IV is accompanied by a jumplike decrease in C_{11} at T_N and a pronounced softening of the shear elastic constant C_{44}. This softening of C_{44} shows a tendency to a monoclinic phase which could become stable if C_{44} would completely soften at T_N. The concentration vs temperature

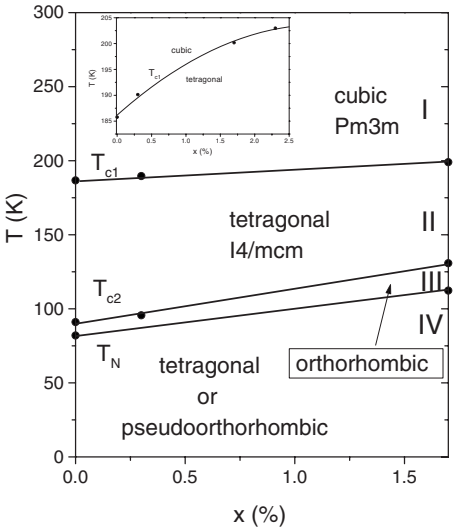

FIG. 4. $x-T$ phase diagram of $KMn_{1-x}Ca_xF_3$ determined from the present high-frequency elastic constants. The inset shows the highly nonlinear dependence of T_{c1} on chemical composition (Refs. 22 and 23).

phase diagram of $KMn_{1-x}Ca_xF_3$ ($x \leq 0.017$) obtained from our CWR measurements is presented in Fig. 4. The increase per mol % Ca for the tree phase transitions are 7.4 K/% for T_{c1}, 23.8 K/% for T_{c2}, and 17.4 K/% for T_N. The values are slightly above those found by Gibaud *et al.*[18] from high-resolution x-ray scattering measurements, where the shifts are 5.8 K/%, 18.0 K/%, and 14.0 K/%, respectively. But it agrees exactly with Ref. 25 for $T_{c1}(x)$.

B. Elastic properties in the Hz region

The elastic behavior of $KMnF_3$ and $KMn_{1-x}Ca_xF_3$ crystals in the Hz region differs drastically from the ultrasonic properties in the MHz region.

Figures 6 and 7 show the temperature dependences of the relative real part $S'_{11} \equiv S'_{11}(T)/S'_{11}(200\ \mathrm{K})$ and imaginary part S''_{11} of the complex elastic compliance of $KMn_{0.997}Ca_{0.003}F_3$ and $KMn_{0.983}Ca_{0.017}F_3$ measured by the DMA method at $f=9$ and 13 Hz, respectively. The dynamical compression in the PPS mode was applied along the [100] direction. Note that these figures show the compliance S_{11}, which is related to the elastic constants by inversion, e.g., $S_{11} := (C^{-1})_{11}$. For transparency we have plotted the relative Young's modulus $Y'[100] := 1/S'_{11}$ and C_{11}, measured at 9 Hz and 15 MHz, respectively (Fig. 5). Strictly speaking these curves cannot be directly compared since generally $1/S_{11} \neq C_{11}$. However, as shown in Fig. 13, $C_{12} \ll C_{11}$ for $KMnF_3$ and therefore one can use $C_{11} \approx 1/S_{11}$ for semiquantitative arguments. The elastic compliance for the mixed compounds with $x=0.003$ and $x=0.017$ increases strongly at T_{c1} (Figs. 6 and 7), quite similar to that observed in the isostructural $SrTiO_3$ crystal.[8,9] This strong increase in the elastic compliance means, that the corresponding Young's modulus $Y := 1/S'_{11}$ softens by about 70% in phase II, an amount which by far exceeds the changes in the elastic constants observed in the MHz region, and the shape of the low-frequency curve is strikingly different from the high-frequency one (Fig. 5). Similar to $SrTiO_3$, we claim that this superelastic softening in $KMnF_3$ and $KMn_{1-x}Ca_xF_3$ is due to the motion of ferroelastic domain walls. However, in contrast to $SrTiO_3$, in $KMn_{1-x}Ca_xF_3$ superelasticity disappears at low temperatures. This happens for quite different reasons in the $x=0.003$ and $x=0.017$ mixed crystals: (i) in highly doped $KMn_{0.983}Ca_{0.017}F_3$, superelasticity vanishes due to the phase transformation from the tetragonal phase II to the orthorhombic phase III at $T=T_{c2}$ (Fig. 7). To explain this feature, one assumes that if there are domains at all in phase III and IV, they must be insensitive to the applied stress in this geometry.

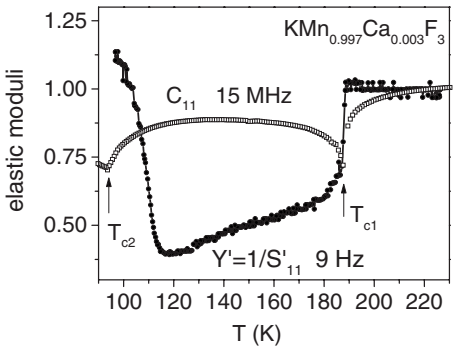

FIG. 5. Comparison of the elastic modulus C_{11} ($f=15$ MHz) and the Young's modulus $Y' := 1/S'_{11}$ ($f=9$ Hz). Both curves are normalized at $T=200$ K.

The giant anomalous softening which appears immediately below T_{c1} can be easily suppressed by external static stress (dc component of stress) applied in the same direction as the measuring ac-stress component (Fig. 7). Particularly, in the case of rather high values of static loads (2150 mN), S'_{11} shows a weak increase (about 20%) below T_{c1}. This value is very close to the anomaly observed in ultrasonic measurements and approximately resembles the mon-

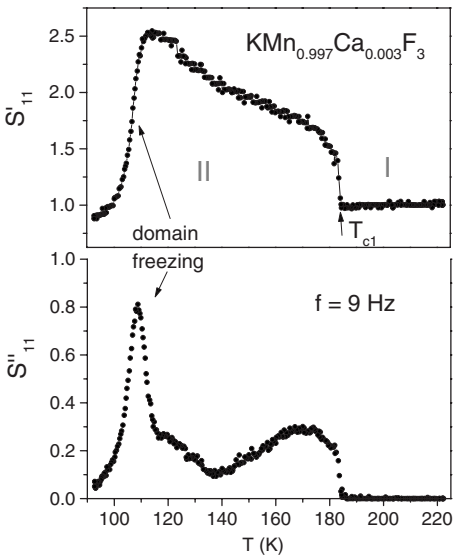

FIG. 6. Temperature dependence of the real S'_{11} and imaginary parts S''_{11} of the complex elastic compliance S^*_{11} of $KMn_{0.997}Ca_{0.003}F_3$ crystals measured by the PPS method at $f=9$ Hz. Both curves are normalized at $T=200$ K.

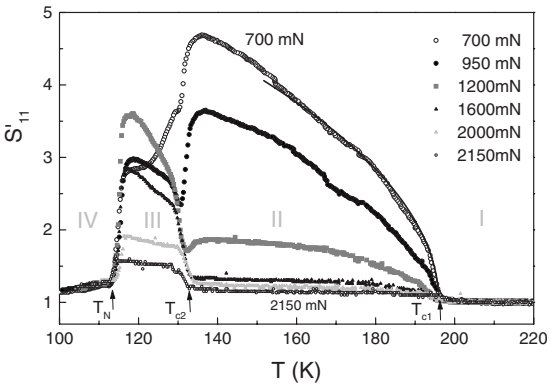

FIG. 7. Temperature dependences of $S'_{11}=S'_{11}(T)/S'_{11}(200\ \mathrm{K})$ of $KMn_{0.983}Ca_{0.017}F_3$ crystals at different static loads $F_S=700-2150$ mN (dynamic load $F_D=600$ mN and $f=13$ Hz). The line shows a fit with Eq. (19).

odomain elastic behavior. The strong influence of external stress on the elastic behavior in phase II confirms the assumption of domain-wall induced softening below T_{c1}. Below we will calculate the stress dependence of the domain-wall contribution to the elastic compliance. Figure 7 also shows, that S'_{11} in phase IV takes the same value as in phase I and is practically unaffected by the applied static load. This also indicates a different domain configuration in this phase with respect to phase II. A similar behavior was recently observed for $Ca_{1-x}Sr_xO_3$ (Ref. 31) and for $SrZrO_3$,[32] where the *Pnma* phase recovers the same stiffness as the *Pm*3*m* paraphase. (ii) For $KMn_{0.997}Ca_{0.003}F_3$ the pronounced low-temperature anomaly around 105 K (Fig. 6) in the real and imaginary parts of the elastic compliance is not related to any phase transition since this temperature range is free of any phase transition for this concentration: Figs. 4 and 5 show, that $T_{c2}(x=0.003)=95$ K. Moreover, the anomalies in both, S'_{11} and S''_{11} are strongly frequency dependent (Fig. 8). With decreasing frequency they shift to lower temperatures. This behavior is reminiscent of a *freezing of the domain-wall motion*.

In the following we will calculate the elastic behavior of $KMnF_3$ and extract the contribution of domain-wall motion to the low-frequency elastic response. Here we will concentrate on the 110 K freezing while the 160 K anomaly was already explained by Salje and Zhang[3] by an extended Debye relaxation with a fairly narrow distribution of activation energies near 0.43 eV.

IV. MODELING THE ELASTIC ANOMALIES

A. Landau theory

In the following, the discussion of the elastic properties of $KMnF_3$ will be limited to an analysis near the cubic-tetragonal transition at T_{c1}. Let us consider the relevant part of the free energy[31,33]

$$F = F_q + F_{\mathrm{el}} + F_c, \tag{5}$$

$$F_q = \frac{1}{2}A(T)(q_1^2+q_2^2+q_3^2) + \frac{1}{4}b_1(q_1^2+q_2^2+q_3^2)^2 + \frac{1}{4}b_2(q_1^4+q_2^4+q_3^4) + \frac{1}{6}c(q_1^2+q_2^2+q_3^2)^3 + \frac{1}{6}c'(q_1q_2q_3)^2 + \frac{1}{6}c''(q_1^2+q_2^2+q_3^2)(q_1^4+q_2^4+q_3^4),$$

$$F_{\mathrm{el}} = \frac{1}{4}(C_{11}^\circ - C_{12}^\circ)(e_\circ^2+e_t^2) + \frac{1}{6}(C_{11}^\circ + 2C_{12}^\circ)e_a^2 + \frac{1}{2}C_{44}^\circ(e_4^2+e_5^2+e_6^2),$$

$$F_c = \lambda_1 e_a(q_1^2+q_2^2+q_3^2) + \lambda_2[\sqrt{3}e_\circ(q_2^2-q_3^2) + e_t(2q_1^2-q_2^2-q_3^2)] + \lambda_3(e_6q_1q_2+e_5q_1q_3+e_4q_2q_3), \tag{6}$$

where $A(T)=\frac{1}{2}\theta A_\circ[\coth(\theta/T)-\coth(\theta/T_\circ)]$, and the symmetry adapted strains are $e_\circ=(e_1-e_2)$, $e_t=(2e_3-e_1-e_2)/\sqrt{3}$ and $e_a=(e_1+e_2+e_3)$. The Debye temperature θ of $KMnF_3$ has been determined[4] as $\theta\approx 400$ K. b_1, b_2, c, c', c'' are expansion coefficients assumed to be temperature independent and λ_1, λ_2, λ_3 are coupling coefficients between the order-parameter components q_1, q_2, q_3 and the strains. C_{ij}° represent the "bare" elastic constants of the cubic phase. The symmetry change $Pm3m \rightarrow I4/mcm$ requires for the order-parameter components $q_1\neq 0$, $q_2=q_3=0$, with the equilibrium order parameter $q_1 := \eta$. From the equilibrium

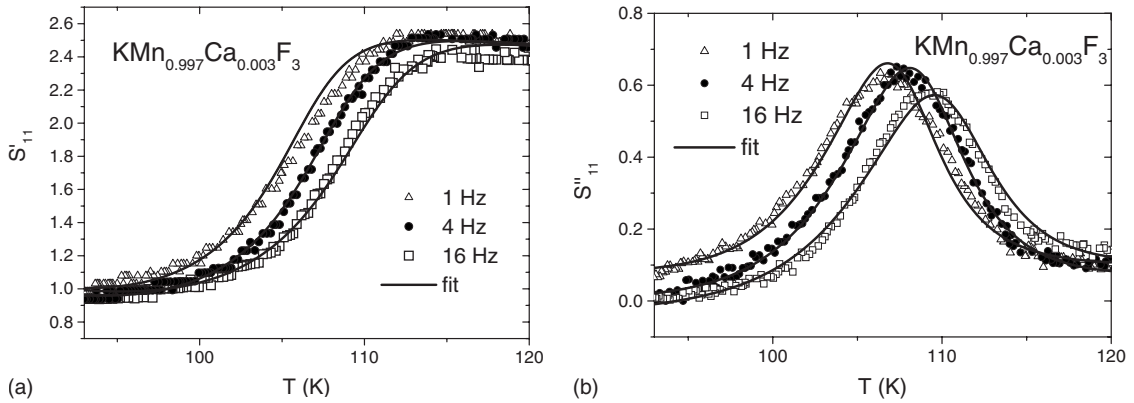

FIG. 8. Temperature dependences of the real S'_{11} and imaginary S''_{11} parts of the elastic compliance of $KMn_{0.997}Ca_{0.003}F_3$ crystals in the vicinity of domain freezing at various frequencies (static load $F_S=220$ mN and dynamic load $F_D=180$ mN). The lines are fits with Eq. (25).

conditions $\partial F/\partial e_i=0$ one obtains for the strains

$$e_a = -\frac{3\lambda_1(q_1^2+q_2^2+q_3^2)}{C_{11}^\circ+2C_{12}^\circ} = -\frac{3\lambda_1\eta^2}{C_{11}^\circ+2C_{12}^\circ},$$

$$e_t = -\frac{2\lambda_2(2q_1^2-q_2^2-q_3^2)}{C_{11}^\circ-C_{12}^\circ} = -\frac{4\lambda_2\eta^2}{C_{11}^\circ-C_{12}^\circ}. \quad (7)$$

Substituting e_a and e_t into the free energy Eq. (6) we obtain the renormalized free-energy expansion

$$F = \frac{1}{2}A(T)\eta^2 + \frac{1}{4}B\eta^4 + \frac{1}{6}C\eta^6, \quad (8)$$

where

$$B = b_1 + b_2 - \frac{6\lambda_1^2}{C_{11}^\circ+2C_{12}^\circ} - \frac{16\lambda_2^2}{C_{11}^\circ-C_{12}^\circ},$$

$$C = c + c''. \quad (9)$$

Minimizing the free energy with respect to the order parameter yields the equilibrium value of the order parameter η

$$\eta^2 = \frac{-B+\sqrt{B^2-4CA(T)}}{2C}, \quad (10)$$

where $T_{c1}=T_o+\frac{3B^2}{16A_oC}$.

The behavior of the static isothermal elastic constants C_{ij} can be derived using the Slonczewski-Thomas equation[34]

$$C_{ij} = C_{ij}^\circ - \sum_{kl}\frac{\partial^2 F}{\partial q_k\,\partial e_i}\left(\frac{\partial^2 F}{\partial q_k\,\partial q_l}\right)^{-1}\frac{\partial^2 F}{\partial q_l\,\partial e_j} \quad (11)$$

yielding

$$C_{11} = C_{22} = C_{11}^o - \frac{2(\lambda_1-2\lambda_2/\sqrt{3})^2}{b_1+b_2+2C\eta^2},$$

$$C_{33} = C_{11}^o - \frac{2(\lambda_1+4\lambda_2/\sqrt{3})^2}{b_1+b_2+2C\eta^2},$$

$$C_{12} = C_{12}^o - \frac{2(\lambda_1-2\lambda_2/\sqrt{3})^2}{b_1+b_2+2C\eta^2},$$

$$C_{13} = C_{23} = C_{12}^o - \frac{\lambda_1^2-2\lambda_1\lambda_2/\sqrt{3}-8\lambda_2^2/3}{b_1+b_2+2C\eta^2},$$

$$C_{44} = C_{55} = C_{44}^o - \frac{\lambda_3^2}{24\lambda_2^2/(C_{11}^o-C_{12}^o)-b_2-2c''^2},$$

$$C_{66} = C_{44}^o. \quad (12)$$

Note that here the unrenormalized coefficients b_1, b_2 enter the elastic anomalies. The experimental data presented in Figs. 1–3 are broadly consistent with the predicted variations in Eq. (12): The temperature dependences of the elastic constants C_{11} (Fig. 1) and $C_{\rm eff}$ (Fig. 2) are characterized by a jumplike decrease at $T=T_{c1}$ followed by an increase with decreasing temperature in agreement with the contributions of the second terms of Eq. (12) in the corresponding elastic constants. However, in the cubic phase all measured elastic constants show a marked precursor softening as T_{c1} is approached from above over a temperature interval of $\approx$50 K for C_{11} and $\approx$20 K for C_{44} (Figs. 1–3). This rounding was also measured by several other authors[3,4,6,15,16] and was attributed to thermal order-parameter fluctuations, i.e., $\Delta C_{ij}^{fl} \propto (T-T_{c1})^{-K}$. Salje *et al.*[3] analyzed the precursor softening in $KMnF_3$ and $KMn_{1-x}Ca_xF_3$ crystals for DMA three-point-bending and ultrasonic data[4] showing that the temperature interval of the precursor softening increases with increasing frequency but the corresponding exponent K is independent of frequency and takes an average value of $K\approx 0.5$. We are not analyzing the fluctuation contribution to the elastic susceptibilities in detail in the present work but qualitatively we find the same frequency behavior of the precursor softening, i.e., no rounding above T_{c1} for PPS measurements at 9 Hz (Figs. 5 and 6) and a pronounced curvature above T_{c1} for CW measurements at 15 MHz (Figs. 1–3).

In contrast to the longitudinal modes, the measured shear elastic constant C_{44} shows only a jumplike decrease and a small cusp at T_{c1} (Fig. 3) which is also in very good agreement with Eq. (12). To fit the data, the Landau parameters A_o, B, C, and the coupling constants λ_1, λ_2 and λ_3 have been determined using the results of thermal expansion[18] and calorimetric measurements.[14,23] Following the procedure described in Ref. 9 yields $A_o=3$ J/K mol$=6.77\times10^{-5}$ GPa/K, $B=-50$ J/mol$=-00011$ GPa, $C=540$ J/mol$=0.0122$ GPa, $\lambda_1=6555$ J/mol$=0.148$ GPa, $\lambda_2=-11830$ J/mol$=-0.267$ GPa, and $\lambda_3=5669$ J/mol$=0.128$ GPa.[35] Using Eq. (9) one obtains $b_1+b_2=614$ J/mol$=0.014$ GPa.

Before fitting the data of the elastic constants one has to be aware of the following facts: there are several sources for deviations from simple mean-field results as given by Eqs. (12). As already mentioned above order-parameter fluctuations have not been taken into account in the present approximation. Moreover the calculated elastic constants are static ones, i.e., they are calculated in the isothermal limit $\omega\tau_{th}\ll 1$ ($\omega=2\pi f$, where f is the frequency of the sound wave and τ_{th} is the thermal relaxation time) as well as for $\omega\tau_\eta\ll 1$, where τ_η is the order-parameter relaxation time. The critical dynamics in $KMnF_3$ near T_{c1} has been measured by ultrasonics[6] yielding an order-parameter relaxation time $\tau_\eta=9\times10^{-13}[(T-T_{c1})/T_{c1}]^{-1.41}$ s above T_{c1} and $\tau_\eta=4\times10^{-14}[(T-T_{c1})/T_{c1}]^{-1.41}$ s below T_{c1}. This implies that the relation $\omega\tau_\eta\ll 1$ is fulfilled for ultrasonic (15 MHz) and DMA (0.1–50 Hz) frequencies in the whole measured temperature range, and this relaxation process does not affect the dynamic susceptibility in Eq. (11).

However, an estimation of the thermal relaxation time $\tau_{th}(q)=1/D_{th}q^2\approx 2\times10^{-2}$ s for $D_{th}=0.002$ cm^2/s of $KMnF_3$ (Ref. 21) and $q=2\pi/\lambda=151$ cm^{-1} for an ultrasonic wavelength of $\lambda=0.04$ cm, yields $\omega_{US}\tau_{th}=2\times10^6\gg 1$, implying that at 15 MHz the elastic constants are the adiabatic ones. Quite generally for varying measurement frequency there is a crossover of the dynamic elastic behavior from the isothermal limit ($\omega\tau_{th}\ll 1$) to the adiabatic ($\omega\tau_{th}\gg 1$) one.[10,36] Moreover, since the thermal relaxation time depends

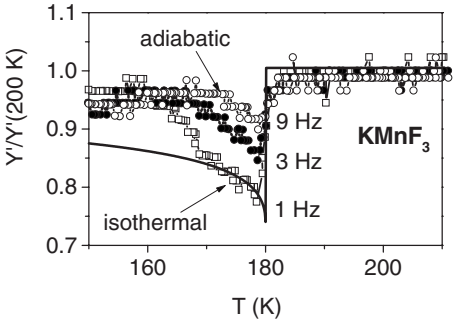

FIG. 9. Temperature dependence of the real part of the Young's modulus Re $Y^r[100]=1/S'_{11}$ of pure $KMnF_3$ in the phase-transition region measured by the PPS method at various frequencies (static load $F_S=300$ mN and dynamic load $F_D=270$ mN). The crossover from isothermal (1 Hz) to adiabatic (9 Hz) behavior is clearly observed. The line shows the calculation of the Young's modulus with Eqs. (12).

strongly on the wavevector q, for a PPS experiment[10] $\tau_{th}(q)\approx 0.1$ s, which is an order of magnitude higher as compared to the value for the CWR experiment. Consequently the isothermal→adiabatic crossover can be measured by dynamic mechanical analysis by varying the frequency in the Hz region. By chance it happened that one of the pure $KMnF_3$ crystals remained in a monodomain state when passing the $Pm3m \rightarrow I4/mcm$ phase transition and hence we could measure the crossover from isothermal ($\omega\tau_{th}=0.6<1$) to adiabatic ($\omega\tau_{th}=5.6>1$) behavior when sweeping the measurement frequency from 1 to 9 Hz (Fig. 9).

The difference between adiabatic and isothermal elastic constants can be calculated from the Pippard relations[37] as

$$(C^{-1T})_{ij} = (C^{-1S})_{ij} + \frac{T\alpha_i\alpha_j}{C_p}, \tag{13}$$

where α_i are the thermal-expansion coefficients and C_p is the specific heat at constant pressure. Using the experimental data for α_i (Ref. 18) and C_p (Ref. 23) we have calculated the

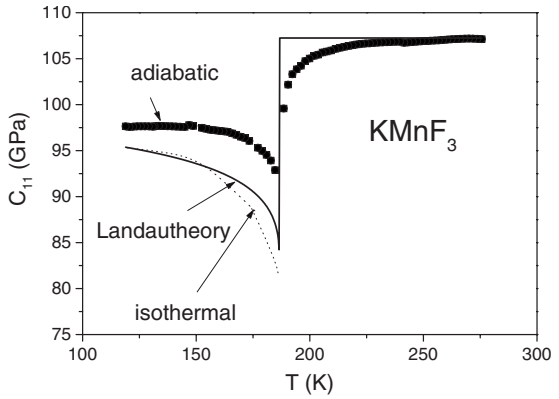

FIG. 10. Full boxes represent the temperature dependence of C_{11} measured by the CWR method (adiabatic limit). Points are isothermal values of C_{11} calculated from Pippard relations (13). The line is a fit using Landau theory, Eqs. (12) and (10). Additional precursor effects above the transition are described in the text.

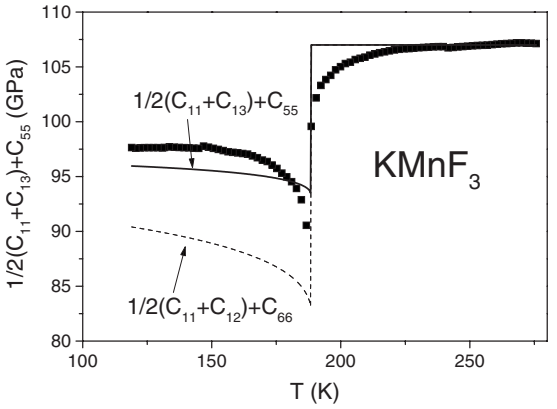

FIG. 11. Temperature dependence of $C_{\text{eff}}=\frac{1}{2}(C_{11}+C_{13})+C_{55}$ determined by the CWR method, and fitted by Landau theory, Eqs. (12) and (10). Additional precursor anomalies above the transition are described in the text.

difference between the isothermal and adiabatic elastic constants to be about 10% at T_{c1}. This agrees very well with our low-frequency elastic measurements (Fig. 9), where the isothermal and adiabatic anomalies are about 25% and 12%, respectively. Moreover, Fig. 10 shows that the high-frequency elastic constant C_{11} can be well fitted by Landau theory if this difference between the adiabatic and isothermal elastic constants is taken into account. Note that the isothermal-adiabatic difference there is also about 10%.

Figure 11 shows that according to the present results C_{eff} most likely corresponds to the combination $C_{\text{eff}}=\frac{1}{2}(C_{11}+C_{13})+C_{55}$. Since in Eq. (12)—which describes the anomaly in C_{44}—only the parameters b_2 and c'' enter, one obtains from the fits of C_{44} (Fig. 12) the values of the following parameters: $b_2=221.5$ J/mol=0.005 GPa, yielding then $b_1=392.5$ J/mol=0.009 GPa and $c''=11.5$ J/mol=0.00026 GPa, yielding $c=528.5$ J/mol=0.0119 GPa.

Summarizing, the high-frequency elastic response near the cubic-tetragonal transition of $KMnF_3$ can be rather well fitted within Landau theory, where the Landau parameters are consistent with the values determined recently by Romero *et al.*[23] Figure 13 summarizes the variations in the

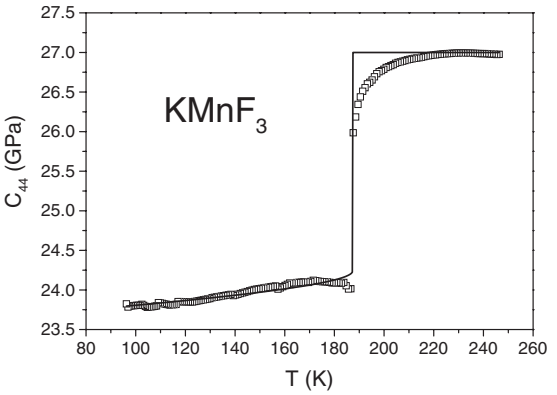

FIG. 12. Temperature dependence of C_{44} determined by the CWR method for transverse mode fitted by Landau theory, Eqs. (12) and (10). Additional precursor anomalies above the transition are described in the text.

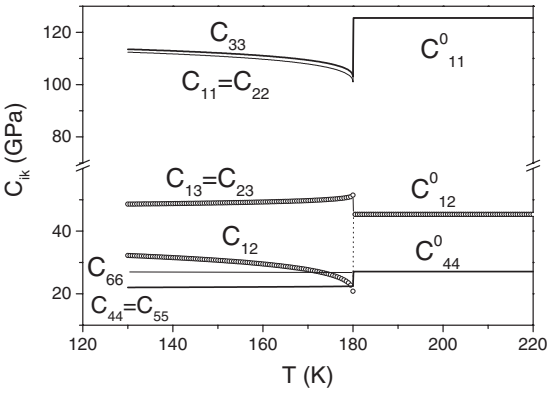

FIG. 13. Variation in the elastic constants of $KMnF_3$ in the vicinity of the cubic-tetragonal phase transition calculated from Landau theory using Eqs. (12) and (10).

elastic constants of $KMnF_3$ near the cubic-tetragonal phase transition, calculated from Eqs. (12).

In principle, domain-wall motion could also blur the high-frequency elastic measurements in the tetragonal phase. However, the present analysis shows that the elastic properties in the MHz regime seem not to be influenced by the presence of domains. This can be easily understood in the light of the very recent three-point bending measurements of Salje *et al.*[3] According to these results, the domain-wall movement in $KMnF_3$ follows an extended Debye relaxation with the relaxation time $\tau_{DW}=8\times10^{-15}\times\exp(0.43\ \mathrm{eV}/k_BT)$. About 1 K below T_{c1} this yields $\tau_{DW}=0.004$ s implying $\omega_{US}\tau_{DW}\approx4\cdot10^5\gg1$, i.e., on the time scale of the CWR experiment the domains are "frozen" and so the MHz data are not affected by domain-wall motion, in agreement with our observations.

In contrast to the MHz data there is an effect of the domain-wall dynamics on the low-frequency elastic behavior of $KMnF_3$ and mixed crystals since $\omega\tau_{DW}\approx0.02-1$ at the frequencies of 1–50 Hz and thus the domain walls can easily follow the applied dynamic stress (Figs. 6 and 8). In the following we will calculate the contribution of domain-wall movement to the dynamic elastic response of $KMnF_3$.

B. Domain-wall contribution to the low-frequency elastic compliance

The influence of domain walls on macroscopic elastic[11,38–40] and dielectric properties[41–44] of materials is a matter of active experimental and theoretical research and is far from being completely understood. The symmetry reduction $Pm3m\rightarrow I4/mcm$ which belongs to the ferroic species $m3mF4/mmm$ leads to three possible domain states, say O_1, O_2, O_3, where the spontaneous strains $\boldsymbol{\epsilon}_s(O_i)$ are in Voight notation given as[45]

$$\boldsymbol{\epsilon}_s(O_1)=(\epsilon_s,\epsilon_s,-2\epsilon_s,0,0,0),$$

$$\boldsymbol{\epsilon}_s(O_2)=(-2\epsilon_s,\epsilon_s,\epsilon_s,0,0,0),$$

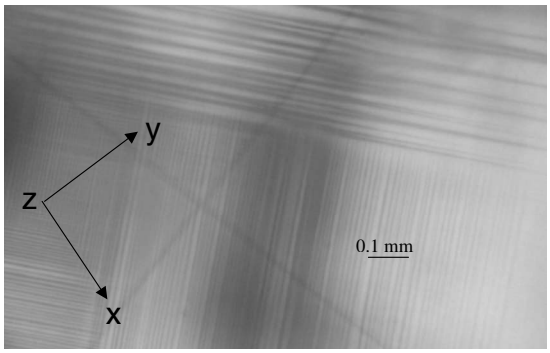

FIG. 14. Needle-shaped ferroelastic domains in $KMn_{0.983}Ca_{0.017}F_3$ at $T=183$ K. The domain walls are oriented in [110] and $[\bar{1}10]$, respectively.

$$\boldsymbol{\epsilon}_s(O_3)=(\epsilon_s,-2\epsilon_s,\epsilon_s,0,0,0). \tag{14}$$

Here $\epsilon_s=\sqrt{\frac{2}{3}}(e_1-e_3)=\sqrt{\frac{1}{3}}\frac{a-c}{a_0}<0$ since $c>a$ in the whole tetragonal phase[18] of $KMnF_3$. ϵ_s is related to the symmetry-adapted tetragonal strain component $e_t=\frac{2}{\sqrt{3}}(e_3-e_1)$ of Eq. (7) through $\epsilon_s=-e_t/\sqrt{2}$. $\epsilon_s\approx-6.1\times10^{-3}$ at about 100 K below T_{c1} and approaches zero at T_{c1}.

The permissible orientations of domain walls can be calculated using Sapriel´s approach[46] with the solutions $x=\pm z$ for O_1/O_2, $y=\pm z$ for O_1/O_3 and $x=\pm y$ for O_2/O_3. To calculate the domain-wall contribution to the elastic susceptibility we use a simplified configuration of the domain structure containing only two types of domains, e.g., in O_2 and O_3 states with domain walls oriented in [110] and $[\bar{1}10]$ direction, as shown in Fig. 14.

We have now to distinguish between two types of domain-boundary motion: domain boundaries can shift "sideways" under external stress, i.e., along the normal to their domain boundaries. The second, more common configuration involves the formation of needle domains whereby two domains join inside the crystal and hence eliminate any domain structure in front of the needle tip (Fig. 14). The movement of such needles is that of retraction and progression of the needle tip toward the surface. Note that needles always point to the bulk of the materials and never into the surface.[47] Experimental work on the dynamics of $LaAlO_3$ has shown that the low force pattern of domain movement is exclusively the needle retraction and progression[11] whereas the sideways movement is typical for large applied stresses and usually rather sparse domain structures. Daraktchiev *et al.*[48] identified the relaxational pattern according to the curvature of the needle tip and the distribution of the activation energy depending on the location of the nucleation center with respect to the location of the needle tip. Highly anisotropic materials, such as $KMnF_3$, are expected to display a rather broad distribution of activation energies because of different defects for the sideways movement.

The two different patterns of domain structures and their dynamics also matter for extended domain structures. For large applied force one has to consider the sidewise movement of the domain walls. To calculate the corresponding effective spring constant for an array of ferroelastic twins,

one needs at first the corresponding free-energy expression. However unlike to ferroelectric or ferromagnetic domains the ferroelastic domains are generally speaking metastable objects. Moreover, in contrast to the statements of some other work[41,42] for perfectly planar ferroelastic domain walls, i.e., parallel walls which intersect the crystal completely, there is no elastic interaction which is sufficiently strong to matter in these considerations. As a result one cannot deduce an equilibrium configuration of ferroelastic domains for this case. For specific boundary conditions however Roytburd[49,50] has shown that the crystals can break into ferroelastic domains (e.g., at the phase front of a first-order phase transition) and dynamical restoring forces exist. Similarly one can expect in second-order phase transitions pinning forces related to crystal surfaces which induce ferroelastic domains. For all these cases we find for small values of the bias force in good approximation for the domain-wall-induced supercompliance

$$\Delta S_{11}^{DW} = -N_w \epsilon_s \frac{\partial x}{\partial \sigma_1}, \tag{15}$$

where N_w is the number of domain walls and x describes the movement of the domain wall in response to the applied stress σ_1. Several geometrical models[51] lead to the same conclusions for the retraction and progression of the needle tips

$$\sigma_1 = S_0 L + M\sqrt{L}, \tag{16}$$

where σ_1 is the applied stress and S_0 describes the limiting force, at which the external load starts to displace the twin wall. M is a constant, which does not depend on the length L of the twin. It originates from the surface tension at the end of the needle. With Eq. (16) one obtains

$$\Delta S_{11}^{DW} \propto -\frac{\epsilon_s}{S_0}\left(\frac{M+\sqrt{M^2+4S_0\sigma_1}}{\sqrt{M^2+4S_0\sigma_1}}\right). \tag{17}$$

For $\sigma_1 \to 0$ this reduces to

$$\Delta S_{11}^{DW} \propto -2\frac{\epsilon_s}{S_0}. \tag{18}$$

Since according to Eq. (7) the spontaneous strain $\epsilon_s \propto -\eta^2$ one obtains for vanishing applied stress

$$\Delta S_{11}^{DW} \propto 2\frac{\eta^2}{S_0}. \tag{19}$$

Figure 7 shows an excellent fit of the data for small stress with $S'_{11}=(1+\Delta S^L_{11}+\Delta S^{DW}_{11})$, where the Landau-Khalatnikov contribution ΔS^L_{11} and the domain-wall contribution ΔS^{DW}_{11} are calculated from Eqs. (12) and (19) with Eq. (10).

More generally one would expect strain dependences of ΔS^{DW}_{11} simply because the transmitted force on a domain wall depends on the strain contrast between two adjacent domains. The linear ϵ_s dependence of ΔS^{DW}_{11} is then understood as the first term of a Taylor expansion of the compliance in terms of the spontaneous strain.

We now return to the stress dependence of the compliance in phase II. The graphs in Fig. 7 show that external bias stress decreases S'_{11}, i.e., the crystal hardens. This can be understood by the fact that increasing stress decreases the number N_w of domain boundaries until the crystal becomes monodomain. Accordingly the boundary related softening decreases and S'_{11} assumes ultimately the bulk value. Huang *et al.*[52] have studied the behavior of an array of ferroelastic domains using an Ising-type model with coarse-grained spin variables $s=\pm 1$ coupled to the strain so that the spontaneous strain of each ferroelastic domain is $s\epsilon_s$, i.e., $\pm\epsilon_s$ in adjacent domains. They calculated the stress dependence of the average number n_w of ferroelastic domain walls as

$$n_w = \frac{N\exp(-2\beta E_w)}{\cosh(\beta\sigma\epsilon_s)[\sinh^2(\beta\sigma\epsilon_s)+\exp(-2\beta E_w)]^{1/2}+\sinh^2(\beta\sigma\epsilon_s)+\exp(-2\beta E_w)}, \tag{20}$$

where E_w is the energy density of one domain wall, which approaches zero for $T \to T_c$ and $\beta=1/k_BT$. As shown in Fig. 7 of Ref. 52, Eq. (20) yields a strongly nonlinear decrease in the average number of domain walls n_w with increasing stress σ. Inserting Eq. (20) into Eq. (15) yields the stress dependence of ΔS^{DW}_{11}. For transparency we expand Eq. (20) in terms of σ, yielding

$$\Delta S_{11}^{DW} \approx \frac{\epsilon_s}{1+\sigma^2\epsilon_s^2\dfrac{\exp(-\beta E_w)+1}{2\exp(-2\beta E_w)}+\ldots} \tag{21}$$

which excellently fits the experimental results as shown in Fig. 15.

C. Domain freezing

Several freezing phenomena have been observed. In the three-point bending experiment, freezing of some domain-wall motion occurs in $KMnF_3$ and also in the mixed crystals around 160 K. The relevant pinning of some of the domains was understood for $KMnF_3$ as an extended Debye model with an average activation energy of 0.43 eV. In mixed crystals, a Vogel-Fulcher mechanism with a V-F temperature of 70 K and an activation energy of 0.23 eV was used to fit the data.[3] Both types of analysis showed a distribution of activation energies and hence a distribution of pinning centers as we will describe below. In the current experiments the freezing occurs in $KMn_{0.997}Ca_{0.003}F_3$ near 110 K with parallelepiped measurements. As shown in Figs. 6 and 8, for

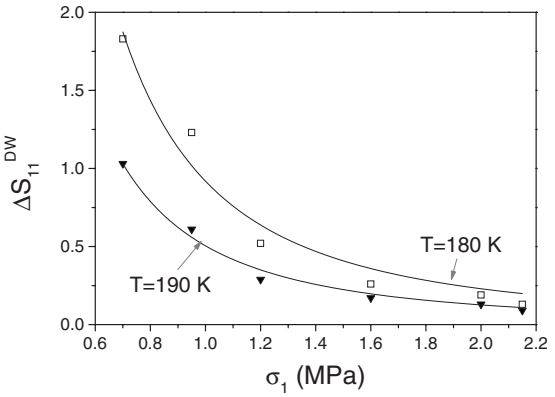

FIG. 15. Stress dependence of the domain-wall contribution to the elastic compliance at two temperatures below T_{c1}. The line shows a fit with Eq. (21).

$KMn_{0.997}Ca_{0.003}F_3$ the elastic compliance recovers around 100 K the value of the high-temperature cubic phase. This occurs due to a freezing (pinning) of the domain-wall motion near a certain temperature T_V. As for glass freezing, we are not aware of any general theory which describes this process, but in a simple picture it is assumed that with decreasing temperature there appears a collective and correlated pinning of the domain walls at randomly distributed defects. As for many glass-forming materials,[53] the temperature dependence of S'_{11} and S''_{11} can be roughly fitted[10] for a given measurement frequency with a Cole-Davidson-type dispersion function $S_{11}(\omega)=S_\infty+\frac{S_0-S_\infty}{(1+\omega\tau)^\nu}$ combined with a Vogel-Fulcher relaxation time $\tau=\tau_0\exp[E_B/(T-T_V)]$. First attempts to fit also the frequency dependence of our experimental data (e.g., of Fig. 8) with this equation yield activation energies of <1 eV while the relaxation time τ_0 is in all cases unphysical, namely, below 10^{-44} s. This result shows clearly that while such standard fits are of good agreement with the experimental data, they do not describe the correct physical picture. To overcome this problem, we resort to the work of Nattermann *et al.*,[54,55] who studied the dynamics of interfaces in random systems. The authors found that in systems with weak pinning the typical potential relief of the interface consists of many metastable minima, separated by energy barriers $E_B(L)$. These energy barriers depend on the length scale of weakly pinned domain-wall segments of length L, i.e.,

$$E_B(L) \propto T_\epsilon (L/L_\epsilon)^\theta, \tag{22}$$

where T_ϵ is the smallest energy barrier between metastable domain-wall positions separated by L_ϵ and $\theta\approx 4/3$ for random-field systems while $\theta\approx 0.83$ for random-bond systems. On macroscopic time scales, i.e., at $t>\tau(L)$, since $\tau(L)=\tau_0\exp[E_B(L)/T]$ the barriers on length L are jumped over and are ineffective for pinning. The minimal scale $L_c(T,t)$, at which the interface is pinned depends therefore on the time scale of the experiment and can be written as[54]

$$L_c \propto \left[1+\frac{T}{T+T_\epsilon}\ln\left(\frac{1}{\omega\tau_0}\right)\right]^{1/\theta}. \tag{23}$$

Over the period of time $t=2\pi/\omega$ only barriers of maximal height $E_B[L_c(\omega)]\propto T_\epsilon[L_c(\omega)/L_\epsilon]^\theta$ can be overcome and contribute to the macroscopic susceptibility. Using Eqs. (22) and (23), this energy barrier, which then is dependent on the time scale (frequency) of the experiment, reads

$$E_B(\omega)=E_0\left[1+\frac{T}{T+T_\epsilon}\ln\left(\frac{1}{\omega\tau_0}\right)\right]. \tag{24}$$

With Eq. (24) and a Cole-Davidson-type dispersion function, we can write the real and imaginary parts of the complex dynamic elastic susceptibility as

$$S'_{11}=S_\infty+(S_0-S_\infty)\frac{\cos[\nu\tan^{-1}(\omega\tau)]}{(1+\omega^2\tau^2)^{\nu/2}},$$

$$S''_{11}=(S_0-S_\infty)\frac{\sin[\nu\tan^{-1}(\omega\tau)]}{(1+\omega^2\tau^2)^{\nu/2}} \tag{25}$$

with

$$\tau=\tau_0\exp\left\{\frac{E_0\left[1+\frac{T}{T+T_\epsilon}\ln\left(\frac{1}{\omega\tau_0}\right)\right]}{T-T_V}\right\}. \tag{26}$$

Figure 8 shows the excellent fit of the data of S'_{11} and S''_{11} with Eqs. (25) and (26). The fit parameters are $(S_0-S_\infty)/S_\infty=1.5$, $\nu=0.5$, $E_0=706$ K, $T_\epsilon=2406$ K, $\tau_0=2\times10^{-15}$ s, and $T_V=55.5$ K. With these parameters the relaxation time τ of domain-wall motion varies between 10^{-3}–10^4 s in the temperature range 120–90 K. Thus at low frequencies (0.1–50 Hz) the domain walls can easily follow the external driving force at sufficiently high temperatures (above $\approx$115 K, see Fig. 8) whereas they become frozen at low temperatures. As already mentioned above, the domain walls cannot follow the external driving force in the MHz range, i.e., $\omega_{US}\cdot\tau=10^4$–$10^{11}\gg1$, in the whole temperature range. Using the above fit parameters in Eq. (24) leads to the following values for the effective energy barriers at the measured frequencies around 100 K: $E_B(1\text{ Hz})=0.14$ eV, $E_B(4\text{ Hz})=0.135$ eV, and $E_B(16\text{ Hz})=0.132$ eV. Although this frequency dependence of the activation energy is weak, it is a crucial factor for fitting the data with meaningful parameters. The assumption of disorder in the model significantly changes the fitted activation energy which makes it very difficult to compare activation energies from different observations directly. Nevertheless, it appears that all experimental observations so far lead to the conclusion of local disorder of various kind, either by extension exponents of the Debye function, which are equivalent to broad distribution functions of the activation energy, or Vogel-Fulcher curves similar to glass formation or, as in our case, the direct assumption of length scale distributions for the movement of domain walls.

The activation energy of (100)-dumbbell fluorine interstitials in $KMnF_3$ was simulated by Kilner[56] to be 0.12 eV and by Becher *et al.*[57] as 0.27 eV. Our value of $E_B\approx0.14$ eV is quite consistent with the former, indicating that the related defects, which pin the domain walls in $KMn_{0.997}Ca_{0.003}F_3$, could be the dumbbell fluorine interstitials. Also the magnitude $\tau_0=2\times10^{-15}$ s is consistent with a point-defect relaxation.[58]

V. SUMMARY

We have performed a comprehensive study of the elastic behavior of pure and mixed fluorperovskites $KMnF_3$ and $KMn_{1-x}Ca_xMnF_3$ in a wide temperature range including three phase transitions, focusing mainly on the cubic—tetragonal phase transition around $T_{c1}=186,5$ K. Strong dispersion effects were observed. A detailed analysis of the data leads to the following picture: At low measurement frequencies ($f=0.1-100$ Hz) the elastic behavior is characterized by a pronounced softening which occurs just below T_{c1} and is related to the movement of ferroelastic twin boundaries. A model which takes into account the extension and retraction of needle-shaped ferroelastic domains in response to the applied stress yields an elastic softening with a magnitude proportional to the spontaneous strain, which itself is proportional to the square of the order parameter. This model fits the data very well for small applied stresses. For higher external stresses, the number of domain walls decreases in a nonlinear way, leading to a nonlinear stress dependence of the domain-wall contribution to the elastic compliance. At very high stress the whole crystal is switched to a (nearly) single-domain state and the elastic compliance approaches the monodomain value.

At ultrasonic frequencies ($f=15$ MHz) the domain walls can no longer follow the stress field and the superelastic softening vanishes. The remaining elastic anomalies can then be well fitted within Landau theory taking into account the coupling terms between the order parameter and the strain components.

For the low-frequency measurements in a certain range of concentration of Ca^{2+} ions (at $x=0.003$) we found a freezing of the domain-wall motion at low temperatures of about 100 K and, as reported earlier, 160 K. This domain freezing, which depends strongly on the measurement frequency, is reminiscent of a glass transition. A model based on the movement of domain walls which are weakly pinned at randomly distributed defects is capable to fit the temperature and frequency dependences of the real and imaginary parts of the elastic compliance very well. Moreover, the activation energy of ≈ 0.14 eV which was obtained from the fits, is very similar to the one which was found theoretically[56] for fluorine interstitials. The physical process, which causes a collective pinning of the domain walls at these randomly distributed defects, leading to a finite Vogel-Fulcher temperature at $T_V \approx 55$ K, remains to be clarified.

ACKNOWLEDGMENTS

The present work was supported by the Austrian FWF Project No. P19284-N20. It was performed in the frame of the *research focus Materials Science "Bulk Nanostructured Materials"* of the University of Vienna.

*wilfried.schranz@univie.ac.at

[1] E. K. H. Salje, Phys. Chem. Miner. **35**, 321 (2008).
[2] I. Jackson, U. F. Faul, J. D. Fitzgerald, and S. J. S. Morris, Mater. Sci. Eng., A **442**, 170 (2006).
[3] E. K. H. Salje and H. Zhang, J. Phys.: Condens. Matter **21**, 035901 (2009).
[4] W. Cao and G. R. Barsch, Phys. Rev. B **38**, 7947 (1988).
[5] E. R. Domb, T. Mihalisin, and J. Skalyo, Phys. Rev. B **8**, 5837 (1973).
[6] R. M. Holt and K. Fossheim, Phys. Rev. B **24**, 2680 (1981).
[7] W. Cao, G. R. Barsch, W. Jiang, and M. A. Breazeale, Phys. Rev. B **38**, 10244 (1988).
[8] A. V. Kityk, W. Schranz, P. Sondergeld, D. Havlik, E. K. H. Salje, and J. F. Scott, Europhys. Lett. **50**, 41 (2000).
[9] A. V. Kityk, W. Schranz, P. Sondergeld, D. Havlik, E. K. H. Salje, and J. F. Scott, Phys. Rev. B **61**, 946 (2000).
[10] W. Schranz, A. Tröster, A. V. Kityk, P. Sondergeld, and E. K. H. Salje, Europhys. Lett. **62**, 512 (2003).
[11] R. J. Harrison, S. A. T. Redfern, and E. K. H. Salje, Phys. Rev. B **69**, 144101 (2004).
[12] V. J. Minkiewicz, Y. Fujii, and Y. Yamada, J. Phys. Soc. Jpn. **28**, 443 (1970).
[13] E. K. H. Salje, M. C. Gallardo, J. Jimenez, F. J. Romero, and J. del Cerro, J. Phys.: Condens. Matter **10**, 5535 (1998).
[14] S. A. Hayward, F. J. Romero, M. C. Gallardo, J. del Cerro, A. Gibaud, and E. K. H. Salje, J. Phys.: Condens. Matter **12**, 1133 (2000).
[15] O. Beckman and R. Knox, Phys. Rev. **121**, 376 (1961).
[16] G. Shirane, V. J. Minkiewicz, and A. Linz, Solid State Commun. **8**, 1941 (1970).
[17] M. Hidaka, M. Ohama, A. Okasaki, H. Sakashita, and S. Yamakawa, Solid State Commun. **16**, 1121 (1975).
[18] A. Gibaud, S. M. Shapiro, J. Nouet, and H. You, Phys. Rev. B **44**, 2437 (1991).
[19] A. J. Heeger, O. Beckman, and A. M. Portis, Phys. Rev. **123**, 1652 (1961).
[20] J. Kapusta, Ph. Daniel, and A. Ratuszna, Phys. Rev. B **59**, 14235 (1999).
[21] A. Salazar, M. Massot, A. Oleaga, A. Pawlak, and W. Schranz, Phys. Rev. B **75**, 224428 (2007).
[22] M. C. Gallardo, F. J. Romero, S. A. Hayward, E. K. H. Salje, and J. D. Cerro, Miner. Mag. **64**, 971 (2000).
[23] F. J. Romero, M. C. Gallardo, S. A. Hayward, J. Jimnez, J. del Cerro, and E. K. H. Salje, J. Phys.: Condens. Matter **16**, 2879 (2004).
[24] A. Gibaud, R. A. Cowley, and J. Nouet, Phase Transitions **14**, 129 (1989).
[25] U. J. Cox, A. Gibaud, and R. A. Cowley, Phys. Rev. Lett. **61**, 982 (1988).
[26] N. Kijima, K. Tanaka, and F. Marumo, Acta Crystallogr. B **39**, 557 (1983).
[27] S. Stokka, K. Fossheim, and V. Samulionis, Phys. Rev. Lett. **47**, 1740 (1981).
[28] D. I. Bolef and M. Menes, J. Appl. Phys. **31**, 1010 (1960).
[29] W. Schranz, Phase Transitions **64**, 103 (1997).
[30] P. Sondergeld, W. Schranz, A. Tröster, M. A. Carpenter, E. Libowitzky, and A. V. Kityk, Phys. Rev. B **62**, 6143 (2000).
[31] M. A. Carpenter, B. Li, and R. C. Liebermann, Am. Mineral. **92**,

344 (2007).
[32] R. E. A. McKnight, C. J. Howard, and M. A. Carpenter, J. Phys.: Condens. Matter **21**, 015901 (2009).
[33] M. A. Carpenter and E. K. H. Salje, Eur. J. Mineral. **10**, 693 (1998).
[34] J. C. Slonczewski and H. Thomas, Phys. Rev. B **1**, 3599 (1970).
[35] Note that λ_1, λ_2 were determined from fitting the strain data of Ref. 18 with Eq. (7) whereas λ_3 was determined from fitting C_{44} with Eq. (12).
[36] A. Tröster and W. Schranz, Phys. Rev. B **66**, 184110 (2002).
[37] S. Haussühl, *Kristallpyhsik* (Deutscher Verlag für Grundstoffindustrie, Leipzig, 1983), p. 307.
[38] R. J. Harrison and S. A. T. Redfern, Phys. Earth Planet. Inter. **134**, 253 (2002).
[39] R. J. Harrison, S. A. T. Redfern, A. Buckley, and E. K. H. Salje, J. Appl. Phys. **95**, 1706 (2004).
[40] C. Wang, S. A. T. Redfern, M. Daraktchiev, and R. J. Harrison, Appl. Phys. Lett. **89**, 152906 (2006).
[41] Y. N. Huang, Y. N. Wang, and H. M. Shen, Phys. Rev. B **46**, 3290 (1992).
[42] Y. N. Huang, X. Li, Y. Ding, Y. N. Wang, H. M. Shen, Z. F. Zhang, C. S. Fang, S. H. Zhuo, and P. C. W. Fung, Phys. Rev. B **55**, 16159 (1997).
[43] Y. N. Wang, Y. N. Huang, H. M. Shen, and Z. F. Zhang, J. Phys. IV **6**, C8-505 (1996).
[44] Th. Braun, W. Kleemann, J. Dec, and P. A. Thomas, Phys. Rev. Lett. **94**, 117601 (2005).
[45] V. K. Wadhawan, Phase Transitions **3**, 3 (1982).
[46] J. Sapriel, Phys. Rev. B **12**, 5128 (1975).
[47] J. Novak, U. Bismayer, and E. K. H. Salje, J. Phys.: Condens. Matter **14**, 657 (2002).
[48] M. Daraktchiev, E. K. H. Salje, W. T. Lee, and S. A. T. Redfern, Phys. Rev. B **75**, 134102 (2007).
[49] A. L. Roytburd, J. Appl. Phys. **83**, 228 (1998).
[50] A. L. Roytburd, J. Appl. Phys. **83**, 239 (1998).
[51] A. M. Kosevich and V. S. Boiko, Sov. Phys. Usp. **14**, 286 (1971).
[52] X. R. Huang, S. S. Jiang, X. B. Hu, X. Y. Xu, W. Zeng, D. Feng, and J. Y. Wang, Phys. Rev. B **52**, 9932 (1995).
[53] J. Koppensteiner, W. Schranz, and M. R. Puica, Phys. Rev. B **78**, 054203 (2008).
[54] T. Nattermann, Y. Shapir, and I. Vilfan, Phys. Rev. B **42**, 8577 (1990).
[55] S. Brazovskii and T. Nattermann, Adv. Phys. **53**, 177 (2004).
[56] J. A. Kilner, Philos. Mag. A **43**, 1473 (1981).
[57] R. R. Becher, M. J. L. Sangster, and D. Strauch, J. Phys.: Condens. Matter **1**, 7801 (1989).
[58] El. M. Bourim, H. Tanaka, M. Gabbay, G. Fantozzi, and B. L. Cheng, J. Appl. Phys. **91**, 6662 (2002).